

# Altermagnetic-Like Behavior and Enhanced Coercivity in Ferrimagnets at a Critical Point of an Extended Néel-Diagram

Qais Ali,<sup>1, 2,\*</sup> Anna Grünebohm,<sup>3</sup> Halil İbrahim Sözen,<sup>4, 5</sup> Tilmann Hickel,<sup>1, 6</sup> Jörg Neugebauer,<sup>1</sup> and Eduardo Mendive-Tapia<sup>7, 8, 9, †</sup>

<sup>1</sup>Department of Computational Materials Design,

Max-Planck-Institut for Sustainable Materials, 40237 Düsseldorf, Germany

<sup>2</sup>Christian Doppler Laboratory for magnet design through physics informed machine learning,  
Department for Integrated Sensor Systems, University for Continuing Education Krems,

Viktor Kaplan-Straße 2E, 2700 Wiener Neustadt, Austria

<sup>3</sup>Interdisciplinary Center for Advanced Materials Simulation,

Center for Interface-Dominated High Performance Materials (ZGH) and Faculty for Physics and Astronomy,  
Ruhr-Universität Bochum, Universitätsstraße 150, 44801 Bochum, Germany

<sup>4</sup>Institute of Chemistry, Carl-von-Ossietzky University of Oldenburg, Oldenburg D-26129, Germany

<sup>5</sup>Mercedes-Benz Turk A.S., Orhan Gazi Mahallesi,

Mercedes Bulvari No. 17/1, Esenyurt, İstanbul 34519, Turkey

<sup>6</sup>BAM Federal Institute for Materials Research and Testing, 12489 Berlin, Germany

<sup>7</sup>Departament de Física de la Matèria Condensada, Facultat de Física,

Universitat de Barcelona, 08028 Barcelona, Catalonia

<sup>8</sup>Institut de Nanociència i Nanotecnologia (IN2UB),

Universitat de Barcelona, 08028 Barcelona, Catalonia, Spain

<sup>9</sup>Institut de Química Teòrica i Computacional (IQTCUB),

Universitat de Barcelona, 08028 Barcelona, Catalonia, Spain

We generalize the classic Néel diagram for ferrimagnets within a mean-field framework and reveal a critical point at which full magnetic compensation is maintained below the Curie temperature and extends past the nominal compensation point. Ferrimagnets tuned to this critical point display altermagnetic-like features and markedly enhanced coercive fields. We show that proximity to this regime requires minimizing the net local moment while balancing exchange interactions with respect to the number of equivalent atoms in each sublattice. The resulting extended Néel diagram provides practical design principles for engineering ferrimagnets near the critical point via targeted chemical substitution that combines atoms with robust and weak local moments, as demonstrated through density functional theory and Monte Carlo simulations for GdCo<sub>5</sub>-type ferrimagnets.

Néel's 1948 work laid the foundation for the theory of ferrimagnets [1]. Smart later refined this framework by developing the well-known Néel diagram, which remains central for interpreting characteristic ferrimagnetic magnetization curves [2]. Ferrimagnets share features of both ferromagnets and antiferromagnets: below the transition temperature from the paramagnetic state  $T_{\text{tr}}$ , they exhibit spontaneous magnetization, yet neighboring ions are antiferromagnetically coupled, yielding two oppositely aligned sublattices [3]. The temperature dependence of this spontaneous magnetization can take forms far more varied than in simple ferromagnets, governed by the magnetic ions in each sublattice and by the molecular-field coefficients [2].

The Néel diagram classifies ferrimagnets into three types: P, Q, and N [2]; see Fig. 1(a). Q-type ferrimagnets resemble ferromagnets, showing a monotonic decrease of magnetization with temperature. In P- and N-type ferrimagnets, however, the sublattices disorder at very different rates. In P-type systems, the sublattice with the

smaller zero-temperature moment decays faster, producing a maximum in the total net magnetization at finite temperature [4, 5]. In N-type systems, the larger-moment sublattice disorders more rapidly, giving rise to a compensation point  $T_{\text{comp}}$  at which the total net magnetization vanishes.

The compensation point in ferrimagnets enables a wide range of applications, with the nearby angular-momentum compensation point playing a key role in the emergence of ultrafast dynamics. Their tunability through chemical composition makes these materials especially promising. Relevant technologies include ultrafast and low-power spintronic devices [6–8], all-optical magnetic switching [9, 10], high-sensitivity magnetic sensors [11], and magnonics [12]. The temperature dependence of intrinsic material properties near the compensation point is an important and active area of research [13, 14].

In this letter we develop an extended Néel's classical diagram, shown in Fig. 1(b), which reveals a previously unreported critical point where the magnetic-moment compensation remains complete over a broad temperature range, akin to antiferromagnets. This critical point provides a framework for understanding and, through chem-

\* Contact author: ali.qais@donau-uni.ac.at

† Contact author: e.mendive.tapia@ub.edu

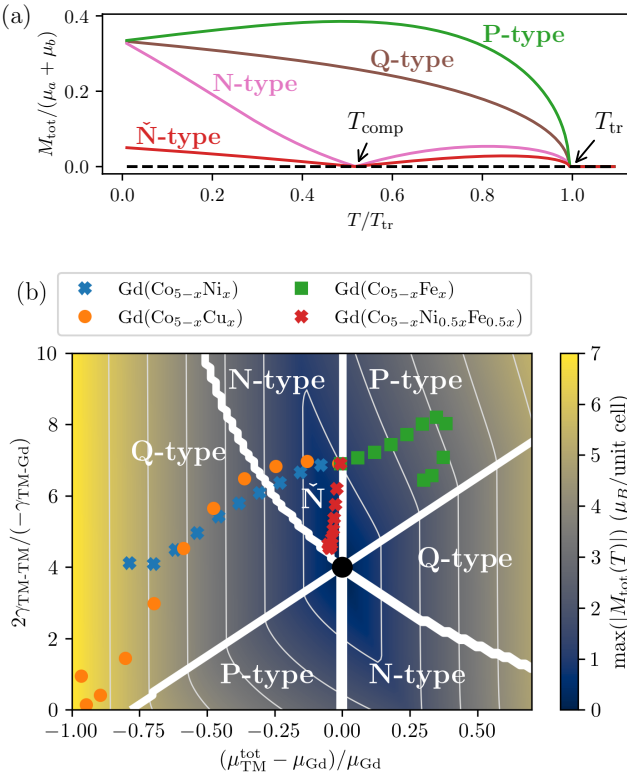


Figure 1. (a) Temperature dependency of the magnetization, normalized to the sum of the two sublattice moment sizes, for P (green), Q (brown) and N-type (pink) typical ferrimagnets with  $\mu_a^{\text{tot}} = 2\mu_b^{\text{tot}}$ . An  $\check{N}$ -type, characterized with a low total magnetization, is also shown. (b) Extended Néel diagram for the total net magnetic moment at zero temperature and the ratio of inter and intralattice interaction  $\gamma_{\text{TM-TM}}/\gamma_{\text{TM-Gd}}$ . All phases meet at the critical point. The color bar indicates the maximum value of the total absolute magnetization. DFT data for ternary and quaternary GdCo<sub>5</sub>-type ferrimagnets are also shown. All data sets originate from  $x = 0$ , corresponding to pristine GdCo<sub>5</sub>. Data points departing from this common origin correspond to progressively larger values of  $x$  in increments of  $\Delta x = 0.5$ .

ical doping, guiding the realization of two key phenomena that arise at the full compensation and are crucial for technological applications.

The first concerns the pronounced increase in coercivity at  $T_{\text{comp}}$ , which serves as a practical marker for approaching the temperature range in which ferrimagnetic dynamics cross over to an ultrafast [15], antiferromagnet-like regime. Prior work has shown that the coercive field peaks at  $T_{\text{comp}}$  in rare-earth alloys [16, 17]. However, how such an enhanced coercivity can be optimized and extended in temperature through modifications of material parameters remains unclear.

Second, we show how a ferrimagnet at the critical point in the new diagram yields a magnetic phase with zero net magnetization together with non-relativistic reciprocal splitting. This places ferrimagnetic materials as

promising alternative candidates capable of exhibiting altermagnetic-like features [18–23]: ultrafast magnetic dynamics and strong (eV-scale) spin-exchange splitting, which underlies phenomena related to spin-splitting currents [24, 25] and torques [24, 26–32], Hall effects [33–35], and giant or tunneling magnetoresistance [36].

A variety of altermagnetic materials have been extensively studied in recent years, including CrSb [37–41], MnTe [34, 42, 43], and RuO<sub>2</sub> [24, 29, 30, 32, 44]. These exhibit vanishing net magnetization at all temperatures due to antiparallel spin alignment protected by combined symmetry operations, typically time reversal followed by a ninety degrees crystal rotation. In contrast, full compensation in ferrimagnets arises from oppositely polarized sublattices that are not related by crystal symmetry, and therefore lie outside the altermagnetism classification [20]. Recent important advances have shown that fully compensated ferrimagnetism with altermagnetic-like features can also appear in two-dimensional filling-enforced systems [45] and in Luttinger-compensated magnetic phases [46]. Our approach differs in the fact that full compensation is achieved through an optimal balance of magnetic-moment magnitudes and exchange interaction ratios via targeted chemical substitution.

The ferrimagnetic systems considered in this work are rare-earth (RE)-transition-metal (TM) GdCo<sub>5</sub>-type compounds. These materials crystallize in the hexagonal CaCu<sub>5</sub>-type structure (space group  $P6/mmm$ ). Investigation of pseudo-binary series, such as Gd(Co<sub>5-x</sub>Ni<sub>x</sub>) [47], reveals a rich compositional dependence in their magnetic behavior, including the change of  $T_{\text{tr}}$ ,  $T_{\text{comp}}$ , and coercive field [16, 17, 48, 49].

*Theoretical framework*—We describe the temperature-dependent magnetic properties of GdCo<sub>5</sub>-type compounds by minimizing their Gibbs free energy obtained by applying a mean-field model [50]:

$$\begin{aligned} \mathcal{G} = & -T[5S_{\text{TM}}(\beta\mathbf{h}_{\text{TM}}) + S_{\text{Gd}}(\beta\mathbf{h}_{\text{Gd}})] + 5K_{\text{TM}}f_u(\beta\mathbf{h}_{\text{TM}}) \\ & - 5\gamma_{\text{TM-Gd}}\mathbf{m}_{\text{TM}} \cdot \mathbf{m}_{\text{Gd}} - 5\gamma_{\text{TM-TM}}m_{\text{TM}}^2 \\ & - \gamma_{\text{Gd-Gd}}m_{\text{Gd}}^2 - \mathbf{B} \cdot (5\mu_{\text{TM}}\mathbf{m}_{\text{TM}} + \mu_{\text{Gd}}\mathbf{m}_{\text{Gd}}), \end{aligned} \quad (1)$$

where  $\beta = 1/k_B T$  is the Boltzmann factor,  $K_{\text{TM}}$  is the value of the uniaxial anisotropy constant at 0 K,  $\mathbf{B}$  is an external magnetic field, and  $\gamma_{\text{TM-TM}}$ ,  $\gamma_{\text{Gd-Gd}}$  quantify the magnetic interactions between and among the TM and Gd sublattices.  $\mathbf{h}_{\text{TM}}$  and  $\mathbf{h}_{\text{Gd}}$  are Weiss fields sustaining magnetic ordering at finite temperature. Their values provide the dependence on temperature of the magnetic entropies,  $S_{\text{TM}}$  and  $S_{\text{Gd}}$ , the order parameters,  $\mathbf{m}_{\text{TM}}(\beta\mathbf{h}_{\text{TM}})$  and  $\mathbf{m}_{\text{Gd}}(\beta\mathbf{h}_{\text{Gd}})$ , and the uniaxial anisotropy function,  $f_u$ , such that all of these quantities depend on  $\beta\mathbf{h}_{\text{TM}}$  and  $\beta\mathbf{h}_{\text{Gd}}$  following the mean-field approximation.  $\mu_{\text{TM}}$  and  $\mu_{\text{Gd}}$  are the corresponding averaged local moment magnitudes,  $\mathbf{M}_{\text{tot}} = \mu_{\text{TM}}\mathbf{m}_{\text{TM}} + \mu_{\text{Gd}}\mathbf{m}_{\text{Gd}}$  being the total magneti-

zation.  $\mathcal{G}$  can be minimized at given values of  $T$  and  $\mathbf{B}$  with respect to the order parameters and self-consistently with  $\mathbf{h}_{\text{TM}}$  and  $\mathbf{h}_{\text{Gd}}$  [5, 50–53]. See Supplemental Material at [54] for additional details.

The model parameters  $\gamma_{\text{TM-TM}}$ ,  $\gamma_{\text{Gd-Gd}}$ ,  $\gamma_{\text{TM-Gd}}$ ,  $\mu_{\text{TM}}$ , and  $\mu_{\text{Gd}}$  can be either introduced phenomenologically or derived from first-principles. We have estimated them for specific Gd(TM<sub>5</sub>)-type ferrimagnets from density functional theory (DFT) calculations.  $\gamma_{\text{TM-TM}}$ ,  $\gamma_{\text{Gd-Gd}}$  and  $\gamma_{\text{TM-Gd}}$  are directly given by the isotropic pairwise interactions  $J_{ij}$  [54], computed using the Liechtenstein method [55]. The anisotropy constants have been set to  $K_{\text{Gd}} = 0$  and  $K_{\text{TM}} = 0.8$  meV [5, 56, 57]. The coherent potential approximation (CPA) [58] has been used to describe chemical disorder at the TM sites [54].

*Extension of the Néel diagram* — We first conduct a general exploration of the ferrimagnetic behaviors that emerge from minimizing  $\mathcal{G}$  over representative parameter choices, including but not limited to those derived from DFT.

The Néel diagrams in Ref. [2] are restricted to cases where the total, zero-temperature, magnetic moment of one sublattice is substantially larger than that of the other, in particular  $\mu_a^{\text{tot}} = 2\mu_b^{\text{tot}}$ . Q, P, and N curves shown in Fig. 1(a) correspond to this typical ferrimagnetic behavior. Consequently, the axes of the diagrams in Ref. [2] were chosen to represent the remaining relevant parameters given by the ratios of effective exchange interactions, i.e.,  $\gamma_{\text{TM-TM}}/\gamma_{\text{TM-Gd}}$  and  $\gamma_{\text{Gd-Gd}}/\gamma_{\text{TM-Gd}}$ . However, this representation is insufficient to explore the potential stabilization of materials with  $\mu_{\text{TM}}^{\text{tot}} \approx \mu_{\text{Gd}}$ , an unexplored and physically interesting case that we address in this work. The resulting ferrimagnetic curve is an extreme instance of an N-type, characterized by an exceptionally low net magnetization for a very large temperature span around the compensation point. This phase is shown in red and labeled as  $\check{N}$ -type in Fig. 1(a).

Our extension of Néel's diagram thus follows by analyzing the different types of ferrimagnetic curves as a function of  $\gamma_{\text{TM-TM}}/\gamma_{\text{TM-Gd}}$  ( $y$ -axis) and, crucially, the total net magnetic moment at zero temperature ( $x$ -axis). The resulting diagram is presented in Fig. 1(b). The effect of  $\gamma_{\text{Gd-Gd}}$  has been neglected. This applies to GdCo<sub>5</sub>-type ferrimagnets, where the interactions satisfy  $\gamma_{\text{Gd-Gd}} \ll \gamma_{\text{TM-TM}}$  and  $\gamma_{\text{Gd-Gd}} \ll 5|\gamma_{\text{TM-Gd}}|$ . For example, in GdCo<sub>5</sub> the respective DFT values that we have computed are  $\gamma_{\text{Gd-Gd}} = 6.3$  meV,  $\gamma_{\text{TM-TM}} = 264$  meV, and  $5\gamma_{\text{TM-Gd}} = -190$  meV. [54] Fig. 1(b) also displays the DFT data for the GdCo<sub>5</sub>-type ferrimagnets under consideration. For  $x = 0$ , all datasets corresponding to the three material series studied, Gd(Co<sub>5-x</sub>TM<sub>x</sub>) with TM = Ni, Fe, or Cu, as well as Gd(Co<sub>5-x</sub>Ni<sub>0.5x</sub>Fe<sub>0.5x</sub>), originate from the same reference point, i.e., the pristine GdCo<sub>5</sub>. Data points progressively departing from this initial point correspond to increasing values of  $x$ .

It is noteworthy that transitions between any two fer-

rimagnetic types are possible. For instance, a P-type phase may transform into either a Q-type or an N-type phase through the emergence of a low-temperature maximum in  $M_{\text{tot}}(T)$  or by the appearance of a compensation point at  $T_{\text{tr}}$ , respectively. When the total magnetic moment on the TM sites exceeds that on the rare-earth site ( $\mu_{\text{TM}}^{\text{tot}} > \mu_{\text{Gd}}$ ), larger values of  $\gamma_{\text{TM-TM}}$  relative to  $|\gamma_{\text{TM-Gd}}|$  favor the stabilization of a P-type phase, while an N-type phase is stabilized when  $\mu_{\text{TM}}^{\text{tot}} < \mu_{\text{Gd}}$ . Opposite trends are observed for large negative values of  $\gamma_{\text{TM-TM}}$ . Moreover, the Q-type phase remains stable for intermediate values of  $\gamma_{\text{TM-TM}}$ .

The critical point at which all phase boundaries converge is generally given by [54]

$$\frac{2(\gamma_{\text{TM-TM}} - \gamma_{\text{Gd-Gd}})}{-\gamma_{\text{TM-Gd}}} = N_{\text{TM}} - N_{\text{Gd}} \quad (2)$$

under the condition  $\mu_{\text{TM}}^{\text{tot}} = \mu_{\text{Gd}}$ . Recall that  $\gamma_{\text{Gd-Gd}} \approx 0$ ,  $N_{\text{TM}} = 5$  and  $N_{\text{Gd}} = 1$  for GdCo<sub>5</sub>-type ferrimagnets, so this critical point occurs at  $2\gamma_{\text{TM-TM}}/|\gamma_{\text{TM-Gd}}| = 4$  in this materials class. Approaching this condition brings the system closer to a fully compensated state at all temperatures [dashed black line in Fig. 1(a)]. The N-type ferrimagnetic configuration with a compensation point and a very small net magnetization over a broad temperature range around it stabilizes in the vicinity of this point.

Fig. 1(b) shows that the difference  $\mu_{\text{TM}}^{\text{tot}} - \mu_{\text{Gd}}$  is negative and decreases further with increasing  $x$  in Gd(Co<sub>5-x</sub>Ni<sub>x</sub>) and Gd(Co<sub>5-x</sub>Cu<sub>x</sub>). This is because Ni and Cu substitution reduces the total magnetic moment at the TM sites. In contrast, substitution with Fe, which carries a strong local moment, markedly enhances  $\mu_{\text{TM}}^{\text{tot}}$ . This observation motivates the exploration of double co-substitution with Ni and Fe, Gd(Co<sub>5-x</sub>Ni<sub>0.5x</sub>Fe<sub>0.5x</sub>), enabling access to the central region of the extended Néel diagram containing the critical point. Indeed, a N-type phase close to the critical point can be stabilized in this quaternary alloy because, for GdCo<sub>5</sub> ( $x = 0$ ),  $\mu_{\text{TM}}^{\text{tot}} \lesssim \mu_{\text{Gd}}$ , and increasing  $x$  preserves this balance: the reduction of the TM moment due to Ni is compensated by the enhancement from Fe. At the same time, the intra-sublattice interaction  $\gamma_{\text{TM-TM}}$  weakens relative to  $\gamma_{\text{TM-Gd}}$  (although both decrease in magnitude), thereby favoring the stabilization of the N-type state closer to the critical point.

We emphasize that the critical-point condition in Eq. (20) is generally applicable to ferrimagnets modeled by two magnetic sublattices. Gd(Co<sub>5-x</sub>Ni<sub>0.5x</sub>Fe<sub>0.5x</sub>) remains unsynthesized but, notably, Stinshoff *et al.* have experimentally realized a quaternary Mn<sub>1.5</sub>FeV<sub>0.5</sub>Al Heusler ferrimagnet exhibiting an N-type configuration very close to the critical point, with a total magnetization below 0.06  $\mu_b/\text{f.u.}$  at all temperatures. They achieved it via Fe and V doping at the Mn 8c and 4b sites [49].

*The coercive field of an  $\check{N}$ -type phase* — Although the N-type ferrimagnetic configuration close to the critical

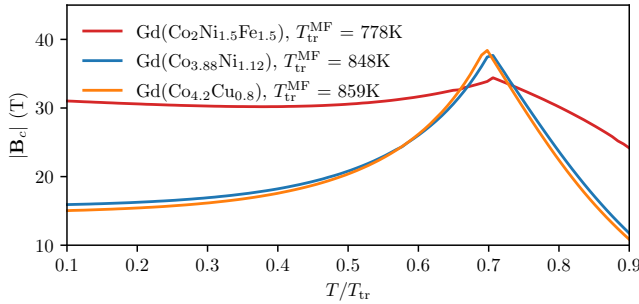


Figure 2. Temperature dependence of coercive fields calculated for selected  $\text{GdCo}_5$ -type ferrimagnets. The temperature axis is normalized to the transition temperature to the paramagnetic state,  $T_{\text{tr}}$ .

point exhibits lower net magnetization values at all temperatures, the behavior of its coercive field is not obvious. To address this, we calculate the temperature dependence of the coercive field by minimizing the mean-field Gibbs free energy given in Eq. (10) under the effect of an applied field. Figure 2 presents the results for selected compositions chosen such that the ratio between the compensation temperature and the transition temperature to the paramagnetic state remains approximately constant across all materials, e.g.,  $T_{\text{comp}}/T_{\text{tr}} \approx 0.7$ . The selected systems are  $\text{Gd}(\text{Co}_2\text{Ni}_{1.25}\text{Fe}_{1.25})$  ( $x = 3$ ), which shows a very small magnetization similar to the N-type curve in Fig. 1(b), as well as  $\text{Gd}(\text{Co}_{3.88}\text{Ni}_{1.12})$  ( $x = 1.12$ ) and  $\text{Gd}(\text{Co}_{4.2}\text{Cu}_{0.8})$  ( $x = 0.8$ ), both representative N-type ferrimagnets. The mean-field values of  $T_{\text{tr}}$  are similar for all three compositions, providing a suitable basis for comparison.

As shown in Fig. 2, the coercive field peaks when the total net magnetization vanishes at  $T_{\text{comp}}$ , which is in agreement with experimental and theoretical findings in rare earth-TM<sub>5</sub> compounds [11, 16, 47, 59, 60]. Due to missing temperature and microstructure and the so-called Landauer's paradox, e.g. missing domain wall motion and thermally activated nucleation, the absolute values for  $B_c$  cannot be compared to experiment.

Interestingly, and somewhat unexpectedly, the estimated  $B_c$  is slightly smaller at  $T_{\text{comp}}$  for  $\text{Gd}(\text{Co}_2\text{Ni}_{1.25}\text{Fe}_{1.25})$  than for the typical N-type phases. However,  $\text{Gd}(\text{Co}_2\text{Ni}_{1.25}\text{Fe}_{1.25})$  exhibits large coercive fields not only in the vicinity of  $T_{\text{comp}}$  but also over a broad temperature range extending from low temperatures up to near  $T_{\text{tr}}$ .  $B_c$  remains large and roughly flat below  $T_{\text{comp}}$ , as also observed experimentally for  $\text{Mn}_{1.5}\text{FeV}_{0.5}\text{Al}$  [49]. Therefore, large coercive fields can be achieved in N-type ferrimagnets over much larger temperature spans, effectively tuned through controlled chemical substitution.

*DFT-informed Monte Carlo simulations, composition-temperature phase diagrams, and exchange spin splitting*

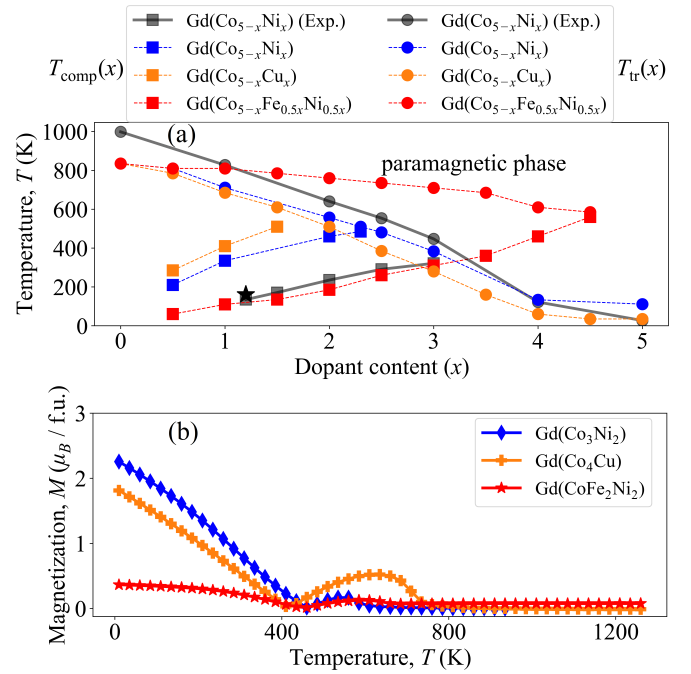


Figure 3. (a) Composition-temperature magnetic phase diagrams obtained for  $\text{Gd}(\text{Co}_{5-x}\text{Ni}_x)$ ,  $\text{GdCo}_{(5-x}\text{Cu}_x)$ ,  $\text{Gd}(\text{Co}_{5-x}\text{Fe}_x)$ , and  $\text{Gd}(\text{Co}_{5-x}\text{Fe}_{0.5x}\text{Ni}_{0.5x})$  by means of Monte Carlo simulations. The compensation temperature,  $T_{\text{comp}}(x)$ , and the transition temperature from the paramagnetic state,  $T_{\text{tr}}(x)$ , are indicated with squares and circles, respectively. Available experimental data for  $\text{Gd}(\text{Co}_{5-x}\text{Ni}_x)$  [16, 47] are also shown in black. The black star shows the value of  $T_{\text{comp}}$  provided by DLM-DFT theory for a  $\text{Gd}(\text{Co}_{5-x}\text{Ni}_x)$  material [16]. (b) Temperature dependence of the total net magnetization for selected compositions of interest.

— The DFT data plotted in Fig. 1(b) were obtained by mapping the isotropic exchange parameters  $J_{ij}$  onto the mean-field model through Eq. (16) in the Supplementary Material [54]. We now show the results of Monte Carlo simulations for  $J_{ij}$  to validate our mean-field predictions. [54]

Fig. 3(a) presents the composition-temperature magnetic phase diagrams constructed from these Monte Carlo simulations, which shows the dependencies of  $T_{\text{comp}}$  and  $T_{\text{tr}}$  on  $x$ . Available experimental data for the case of  $\text{Gd}(\text{Co}_{5-x}\text{Ni}_x)$  is also plotted, demonstrating good agreement between theory and experiment at both qualitative and quantitative levels. The changes observed in the Cu-substituted series,  $\text{Gd}(\text{Co}_{5-x}\text{Cu}_x)$ , progress more rapidly than in the Ni-substituted counterpart, reflecting the smaller perturbation introduced by Ni, whose valence configuration is closer to Co's. The critical substitution levels at which the N-to-Q transition occurs are approximately  $x \approx 2.5$  for  $\text{TM} = \text{Ni}$  and  $x \approx 1.5$  for  $\text{TM} = \text{Cu}$ . In contrast, no such transition is observed for  $\text{Gd}(\text{Co}_{5-x}\text{Ni}_{0.5x}\text{Fe}_{0.5x})$ . These results are in good

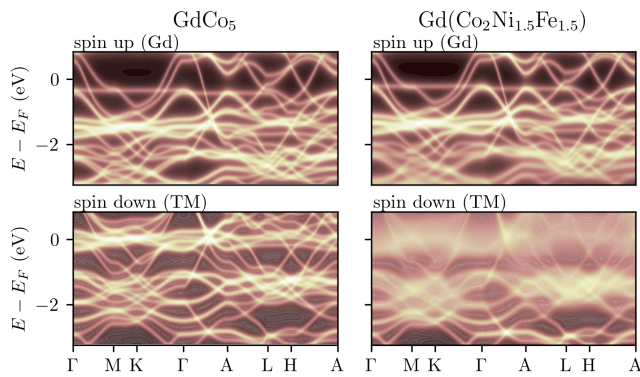


Figure 4. Electronic band structures calculated for GdCo<sub>5</sub> (left) and Gd(Co<sub>2</sub>Ni<sub>1.5</sub>Fe<sub>1.5</sub>) (right) at zero temperature. No spin-orbit coupling is included.

agreement with the mean-field mapping of the DFT data shown in the extended Néel diagram in Fig. 1(b).

Fig. 3(b) shows the total net magnetization for selected values of  $x$  across the three alloy series that display N-type behavior. All of them exhibit similar compensation temperatures around  $T_{\text{comp}} \approx 400$  K, analogous to the case investigated in Fig. 2. While Gd(Co<sub>5-x</sub>Ni<sub>x</sub>) and Gd(Co<sub>5-x</sub>Cu<sub>x</sub>) are typical N-type curves, the quaternary alloy Gd(Co<sub>5-x</sub>Ni<sub>0.5x</sub>Fe<sub>0.5x</sub>) exhibits very small net magnetization over the entire temperature range, in agreement with the mean-field analysis.

Ferrimagnetic compounds very close or at the critical point should exhibit similar altermagnetic characteristics: a vanishing small net magnetization coexisting with a strong spin splitting in the reciprocal space of purely non-relativistic origin. Figure 4 shows the DFT-computed spin-up (Gd) and spin-down (TM) projected bands for GdCo<sub>5</sub>-type ferrimagnets. A large spin splitting of order  $\sim 1$  eV (most clearly visible for GdCo<sub>5</sub>, left panels) arises because TM's and Gd's electrons belong to different chemical sublattices. We note that Gd(Co<sub>2</sub>Ni<sub>1.5</sub>Fe<sub>1.5</sub>), which is very close to the critical point, has an almost vanishing total magnetic moment (below  $|\mu_{\text{tot}}| = 0.04\mu_B$  per primitive cell at all temperatures), while its spin splitting remains essentially identical to that of GdCo<sub>5</sub>. The observed band broadening is caused by the chemical disorder.

*Discussion and conclusions* — We extend Néel's classic diagram of ferrimagnetic compensation behavior to explicitly include the effect of magnetic-moment magnitudes, which reveals a critical point where a ferrimagnet is fully compensated while maintaining strong, eV-scale spin splitting without spin-orbit coupling. Ferrimagnetic materials tuned to this critical point are therefore expected to exhibit spin-splitting currents, THz-scale dynamics, and giant or tunneling magnetoresistance. We note that anomalous Hall effects would still require the presence of spin-orbit coupling, as in altermagnets, or a

non-collinear magnetic structure such as that reported for Mn<sub>4-x</sub>Z<sub>x</sub>N ferrimagnets [61, 62]. Full compensation in ferrimagnets is a fine-tuned cancellation of inequivalent sublattice moments and, therefore, does not generically produce symmetry-protected spin-splitting torques. Importantly, ferrimagnetic curves in the vicinity of the critical point are predicted to show enhanced coercive fields over a broad temperature range, offering pathways for designing permanent magnets with reduced stray fields.

Our predictions are supported by ab initio-informed Monte Carlo simulations for selected ternary and quaternary GdCo<sub>5</sub>-type compounds showing a good agreement of the composition-temperature phase diagram with experiment. The extended Néel diagram applies generally to ferrimagnets composed of primary and secondary sublattices with  $N_a$  and  $N_b$  atoms. Approaching the critical point requires (i) tuning the total local moment toward zero via substitution of weak (e.g., Ni) and strong (e.g., Fe) magnetic atoms while (ii) adjusting the interaction ratio to satisfy  $2(\gamma_{aa} - \gamma_{bb})/(-\gamma_{ab}) = N_a - N_b$ . We expect that our results will stimulate the search for ferrimagnets tuned towards the critical point where altermagnetism-like features and enhanced coercive fields emerge.

*Acknowledgments*—We gratefully acknowledge helpful discussions with C. E. Patrick and J. B. Staunton. E. M.-T. is grateful for financial support from MICIU/AEI/10.13039/501100011033/ and FEDER, UE with Grant. No. PID2024-161052NA-I00, and from CEX2021-001202-M/ AEI/10.13039/501100011033. The authors acknowledge computing time granted by the supercomputer of the Department of Computational Materials Design, operated by the Max Planck Computing and Data Facility in Garching.

*Data availability*—The data are not publicly available. The data are available from the authors upon reasonable request.

## Supplemental Material

### MODELING FRAMEWORK

#### Magnetic Hamiltonian and zero-temperature limit

We model a uniaxial ferrimagnetic material with the following Heisenberg-type Hamiltonian as

$$\mathcal{H} = -\frac{1}{2} \sum_{ij} J_{ij} \hat{\mathbf{e}}_i \cdot \hat{\mathbf{e}}_j + \sum_i K_i [1 - (\hat{\mathbf{e}}_i \cdot \hat{\mathbf{u}})^2] - \mathbf{B} \cdot \sum_i \mu_i \hat{\mathbf{e}}_i, \quad (3)$$

where the factor  $\frac{1}{2}$  removes the double counting,  $\mathbf{B}$  is the applied magnetic field, and  $\{\hat{\mathbf{e}}_i\}$  are classical unit vectors denoting the orientations of the magnetic moments localized at sites  $\{i\}$  with magnitudes  $\{\mu_i\}$ . For positive values of  $K_i$  the magnetic moments tend to align along the easy axis  $\hat{\mathbf{u}}$ . We remark that Eq. (3) does not include dipolar interactions nor higher orders of exchange interactions and of anisotropy coefficients. Their effect is not necessary to obtain the results presented in the main text [5, 57]: the extension of the Néel diagram and the prediction of magnetic transitions in the composition-temperature diagram of GdCo<sub>5</sub>-type ferrimagnets.

We focus on ferrimagnetic materials with two non-equivalent sites  $a$  and  $b$  in the unit cell, with  $N_a$  and  $N_b$  atomic positions and local magnetic moments  $\mu_a$  and  $\mu_b$ , respectively. For the ferrimagnetic state the magnetic unit cell contains  $N_a + N_b$  atoms. The energy per unit cell at zero temperature is

$$E_{0K} = -\gamma_{aa} N_a \hat{\mathbf{e}}_a \cdot \hat{\mathbf{e}}_a - \gamma_{bb} N_b \hat{\mathbf{e}}_b \cdot \hat{\mathbf{e}}_b - \gamma_{ab} N_a N_b \hat{\mathbf{e}}_a \cdot \hat{\mathbf{e}}_b + K_a N_a \sin^2 \theta_a + K_b N_b \sin^2 \theta_b - \mathbf{B} \cdot (N_a \mu_a \hat{\mathbf{e}}_a + N_b \mu_b \hat{\mathbf{e}}_b), \quad (4)$$

where  $K_a$  and  $K_b$  are the uniaxial constants, while  $\theta_a$  and  $\theta_b$  are the angles between moments and easy axes of both sublattices.  $\gamma_{aa}$ ,  $\gamma_{bb}$ , and  $\gamma_{ab}$  come from the isotropic constants  $J_{ij}$ , quantifying the exchange interaction for a ferrimagnetic state among and between the two non-equivalent positions, respectively. Note that at  $T = 0$  K,  $\hat{\mathbf{e}}_a \cdot \hat{\mathbf{e}}_a = \hat{\mathbf{e}}_b \cdot \hat{\mathbf{e}}_b = 1$  and so the first two terms in the right-hand-side of Eq. (4) are mere constants. We, however, write them down here as the presence of  $\gamma_{aa}$  and  $\gamma_{bb}$  at finite temperature is important due to local moment fluctuations, see section .

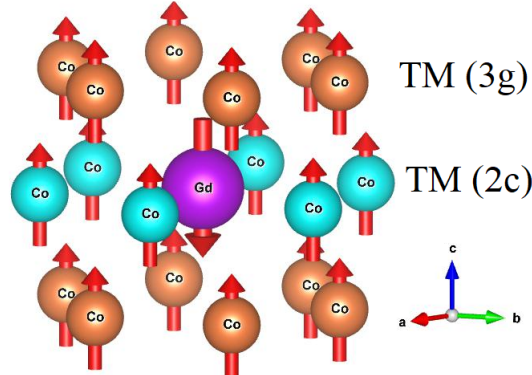


Figure 5. CaCu<sub>5</sub> hexagonal structure of (Gd,TM<sub>5</sub>)-type compounds with a ferrimagnetic ground state. In the unit cell there is one Gd site in purple and two different Wyckoff positions for TM atoms, namely 2c in cyan and 3g in golden brown. These TM sites can be occupied by one or a solution of different TM atoms (e.g., Co, Ni, Cu, Fe).

Along the  $c$  axis, layers of transition-metal (TM) atoms at the 3g Wyckoff site alternate with mixed layers containing Gd and TM atoms at the 2c Wyckoff site, see Fig. 5. We have found that the magnetic properties of the 2c and 3g are very similar. This allows the material to be modeled with  $N_a = N_{\text{TM}} = 5$  (i.e.,  $\hat{\mathbf{e}}_a = \hat{\mathbf{e}}_{\text{TM}}$ ) and  $N_b = N_{\text{Gd}} = 1$  (i.e.,  $\hat{\mathbf{e}}_b = \hat{\mathbf{e}}_{\text{Gd}}$ ). These values are taken throughout the main text.

## On the origin of $\gamma_{aa}$ , $\gamma_{bb}$ , and $\gamma_{ab}$ , and their connection to density functional theory

The relation between  $\{J_{ij}\}$  and  $\gamma_{\text{TM-TM}}$ ,  $\gamma_{\text{Gd-Gd}}$ ,  $\gamma_{\text{TM-Gd}}$  is provided by firstly Fourier transforming the interactions

$$J_{ss'}(\mathbf{q}) = \frac{1}{N_c} \sum_{tt'} \sum_{\alpha\alpha'} J_{tst's'}^{\alpha\alpha'} p_\alpha \cdot p_{\alpha'} \cdot e^{-i\mathbf{q} \cdot (\mathbf{X}_{ts} - \mathbf{X}_{t's'})}, \quad (5)$$

where  $N_c$  is the total number of unit cells in the crystal,  $\mathbf{X}_i = \mathbf{X}_{ts}$  (and  $\mathbf{X}_j = \mathbf{X}_{t's'}$ ) is a vector giving the position of the atoms, and  $\mathbf{q}$  is the wave vector. Here the lattice indices  $i$  and  $j$  are split into two indices,  $ts$  and  $t's'$ , respectively. This allows to decompose the position vector as  $\mathbf{X}_{ts} = \mathbf{R}_t + \mathbf{r}_s$ , where  $\mathbf{R}_t$  and  $\mathbf{r}_s$  are vectors pointing to the origin of the unit cell and to the magnetic atom inside this unit cell with respect to its origin, respectively. Therefore,  $s$  and  $s'$  run over sub-lattice indices while  $t$  and  $t'$  over the unit cell origins.  $p_\alpha$  is the probability of finding atom  $\alpha$  sitting in sublattice  $s$ . For example, for one of our case studies  $\text{GdCo}_{5-x}\text{Ni}_x$ ,  $p_{\text{Gd}} = 1$ ,  $p_{\text{Co}} = (5-x)/5$  and  $p_{\text{Ni}} = x/5$ . Section shows how to derive the values of  $\gamma_{\text{TM-TM}}$ ,  $\gamma_{\text{Gd-Gd}}$ , and  $\gamma_{\text{TM-Gd}}$  from the elements of matrix  $J_{ss'}$  at  $\mathbf{q} = \mathbf{0}$ .

The model parameters  $\gamma_{\text{TM-TM}}$ ,  $\gamma_{\text{Gd-Gd}}$ ,  $\gamma_{\text{TM-Gd}}$ ,  $\mu_{\text{TM}}$ , and  $\mu_{\text{Gd}}$ , together with the uniaxial anisotropy constants, can be either introduced phenomenologically or derived from density-functional theory (DFT) calculations. Two routes can be employed for the latter:

1. Evaluation of  $J_{ij}$  via the Liechtenstein method [55], based on infinitesimal rotations of local moments around a chosen reference magnetic state and application of Eq. (5) and derivations given in .
2. Application of the DFT-based disordered local moment (DLM) framework [63], which directly yields  $\gamma_{\text{TM-TM}}$ ,  $\gamma_{\text{Gd-Gd}}$ ,  $\gamma_{\text{TM-Gd}}$  as Gibbs free energy coefficients in the spirit of a Landau-type expansion [5, 52].

In the main text we analyze the influence of the parameters  $\gamma_{\text{TM-TM}}$ ,  $\gamma_{\text{Gd-Gd}}$ ,  $\gamma_{\text{TM-Gd}}$ ,  $\mu_{\text{TM}}$ , and  $\mu_{\text{Gd}}$  on the Néel diagram using a phenomenological approach. To this end, we construct the general form of the Gibbs free energy  $\mathcal{G}$  inspired by the DLM-DFT framework, presented in section , without performing explicit DLM-DFT calculations. By exploring phenomenological values of the model parameters, we demonstrate how minimizing  $\mathcal{G}$  reproduces and extends Néel's seminal diagram for ferrimagnets. We apply these insights to  $\text{GdCo}_5$ -type materials, including their ternary and quaternary alloys. To this end, we compute the exchange constants  $J_{ij}$  using the Liechtenstein method [55] and estimate the associated Gibbs free energy parameters through Eq. (5), as described in section . The details of these DFT calculations and the subsequent Monte Carlo simulations are given in Secs. and , respectively.

It is worth noting that previous DLM-DFT studies for  $\text{GdCo}_5$ -based ferrimagnets have shown that the terms included in Eq. (4) suffice to describe their magnetic behavior [5]. Further discussion of their connection to the microscopic Hamiltonian [Eq. (3)], as well as methods for constructing and minimizing  $\mathcal{G}$ , can be found elsewhere [5, 50, 52, 53].

## Mean-field approach and the DLM-based Gibbs free energy

At finite temperatures, a mean-field approximation for the Hamiltonian in Eq. (3) can be implemented via the Peierls-Feynmann inequality [64, 65]. This requires to introduce a trial Hamiltonian, which is chosen to describe a coupling of the localized local moment orientations  $\{\hat{\mathbf{e}}_{\text{TM}}, \hat{\mathbf{e}}_{\text{Gd}}\}$  with site-dependent molecular fields  $\{\mathbf{h}_{\text{TM}}, \mathbf{h}_{\text{Gd}}\}$  [63]:

$$\mathcal{H}_{\text{tr}} = -N_{\text{TM}} \mathbf{h}_{\text{TM}} \cdot \hat{\mathbf{e}}_{\text{TM}} - \mathbf{h}_{\text{Gd}} \cdot \hat{\mathbf{e}}_{\text{Gd}}. \quad (6)$$

The probability of different local moment configurations associated with  $\mathcal{H}_{\text{tr}}$  factorizes due to the single-site nature of the trial Hamiltonian to

$$P(\{\hat{\mathbf{e}}_{\text{TM}}, \hat{\mathbf{e}}_{\text{Gd}}\}) = \prod_t [P_{t,\text{TM}}(\hat{\mathbf{e}}_{\text{TM}})]^{N_{\text{TM}}} P_{t,\text{Gd}}(\hat{\mathbf{e}}_{\text{Gd}}). \quad (7)$$

Here the index  $t$  labels the unit cells throughout the crystal and the single-site probabilities are given as

$$P_i(\hat{\mathbf{e}}_i) = \frac{1}{Z_{\text{tr},i}} \exp [\beta \mathbf{h}_i \cdot \hat{\mathbf{e}}_i], \quad (8)$$

where the normalization  $Z_{\text{tr},i} = \frac{4\pi \sinh(\beta h_i)}{\beta h_i}$  comes from the calculation of the partition function, and  $\beta = \frac{1}{k_B T}$  is the Boltzmann factor.

The Peierls-Feynmann inequality provides a mean-field based Gibbs free energy that minimizes with respect to the molecular field parameters  $\mathbf{h}_{\text{TM}}$  and  $\mathbf{h}_{\text{Gd}}$ ,  $\mathcal{G} = -TS + H$ , [50, 52] where  $S = N_{\text{TM}}S_{\text{TM}} + S_{\text{Gd}}$  is the total entropy composed of sublattice entropies

$$S_i = k_{\text{B}}\langle -\log P_i \rangle_{\text{tr}} = k_{\text{B}} \left[ 1 + \ln \left( 4\pi \frac{\sinh(\beta h_i)}{\beta h_i} \right) - \beta h_i \coth(\beta h_i) \right], \quad (9)$$

$\langle \dots \rangle_{\text{tr}}$  denoting the thermal average using the trial probability in Eq. (8).  $H$  is the enthalpy, that is, the generalization of Eq. (4) to finite temperature obtained by performing the thermal average of Eq. (3). The corresponding mean-field Gibbs free energy, basis of DLM-DFT theory for magnetic phase transitions, thus is

$$\begin{aligned} \mathcal{G} = & -T(N_{\text{TM}}S_{\text{TM}} + S_{\text{Gd}}) + K_{\text{TM}}N_{\text{TM}}f_u(\beta \mathbf{h}_{\text{TM}}) + K_{\text{Gd}}f_u(\beta \mathbf{h}_{\text{Gd}}) - \gamma_{\text{TM-Gd}}N_{\text{TM}}\mathbf{m}_{\text{TM}} \cdot \mathbf{m}_{\text{Gd}} \\ & - \gamma_{\text{TM-TM}}N_{\text{TM}}m_{\text{TM}}^2 - \gamma_{\text{Gd-Gd}}m_{\text{Gd}}^2 - \mathbf{B} \cdot (N_{\text{TM}}\mu_{\text{TM}}\mathbf{m}_{\text{TM}} + \mu_{\text{Gd}}\mathbf{m}_{\text{Gd}}) \end{aligned} \quad (10)$$

where

$$\mathbf{m}_i = \langle \hat{\mathbf{e}}_i \rangle_{\text{tr}} = \left[ -\frac{1}{\beta h_i} + \coth(\beta h_i) \right] \hat{\mathbf{h}}_i \quad (11)$$

are local magnetic order parameters, while the thermal averages of the anisotropy terms are

$$f_u(\beta \mathbf{h}_i) = \langle \sin^2(\theta_i) \rangle_{\text{tr}} = 1 - \left( \hat{\mathbf{h}}_i \cdot \hat{\mathbf{z}} \right)^2 + \frac{1}{\beta h_i} \left( \frac{-1}{\beta h_i} + \coth(\beta h_i) \right) \left( 3(\hat{\mathbf{h}}_i \cdot \hat{\mathbf{z}})^2 - 1 \right). \quad (12)$$

The temperature-dependent magnetic properties are obtained by minimizing Eq. (10) with respect to  $\{\mathbf{m}_i\}$  (or equivalently  $\{\mathbf{h}_i\}$ ) at different values of  $T$  and  $\mathbf{B}$ .

#### Calculation of the coercive field

A ferrimagnetic ground state is stabilized by  $\gamma_{\text{TM-Gd}} < 0$ ,  $\gamma_{\text{TM-TM}} > 0$ ,  $\gamma_{\text{Gd-Gd}} > 0$ . Its net magnetization is given by  $\mathbf{M}_{\text{tot}} = 5\mu_{\text{TM}}\mathbf{m}_{\text{TM}} + \mu_{\text{Gd}}\mathbf{m}_{\text{Gd}}$ . The coercive field is defined as the magnetic field  $\mathbf{B}_c$ , applied antiparallel to  $\mathbf{M}_{\text{tot}}$ , at which the state ceases to be a local minimum [17]. At finite temperature,  $\mathbf{B}_c$  must be calculated numerically. However, in the zero-temperature limit an analytical expression can be obtained by analyzing the Hessian matrix of  $E_{0K}$  with respect to the two angular variables:

$$\mathbf{B}_c(T = 0 \text{ K}) = \frac{-b - \sqrt{b^2 - 4\mu_{\text{TM}}\mu_{\text{Gd}}c}}{2\mu_{\text{TM}}\mu_{\text{Gd}}}(-\hat{\mathbf{M}}) \quad (13)$$

where  $b = \gamma_{\text{TM-Gd}}(N_{\text{TM}}\mu_{\text{TM}} - \mu_{\text{Gd}}) - 2(K_{\text{Gd}}\mu_{\text{TM}} - K_{\text{TM}}\mu_{\text{Gd}})$  and  $c = -4K_{\text{TM}}K_{\text{Gd}} + 2\gamma_{\text{TM-Gd}}(N_{\text{TM}}K_{\text{TM}} + K_{\text{Gd}})$  if  $N_{\text{TM}}\mu_{\text{TM}} > \mu_{\text{Gd}}$ . Importantly, the coercive field is independent of the magnetic intralattice exchange ( $\gamma_{\text{TM-TM}}$  and  $\gamma_{\text{Gd-Gd}}$ ). If instead  $N_{\text{TM}}\mu_{\text{TM}} < \mu_{\text{Gd}}$ , the coefficient  $b$  changes sign. This sign reversal leads to a discontinuity in the coercive field when  $\mathbf{M}_{\text{tot}}$  flips direction.

#### Relation between real space exchange interactions and free energy magnetic parameters

The size of  $J_{ss'}(\mathbf{q})$ , introduced in Eq. (5), is  $n \times n$ , where  $n$  is the number of atoms inside the primitive cell. Therefore,  $n = 6$  for GdCo<sub>5</sub>-type ferrimagnets. For  $\mathbf{q} = \mathbf{0}$ , the matrix can be generally given by eight different parameters:

$$J_{ss'} = \begin{pmatrix} \alpha_1 & \beta_1 & \gamma & \gamma & \gamma & \epsilon_1 \\ \beta_1 & \alpha_1 & \gamma & \gamma & \gamma & \epsilon_1 \\ \gamma & \gamma & \alpha_2 & \beta_2 & \beta_2 & \epsilon_2 \\ \gamma & \gamma & \beta_2 & \alpha_2 & \beta_2 & \epsilon_2 \\ \gamma & \gamma & \beta_2 & \beta_2 & \alpha_2 & \epsilon_2 \\ \epsilon_1 & \epsilon_1 & \epsilon_2 & \epsilon_2 & \epsilon_2 & \alpha_3 \end{pmatrix}, \quad (14)$$

which reflects the symmetry of the magnetic unit cell. The eigenvector of Eq. (14) with the highest eigenvalue (the most stable magnetic state) that we have found for the materials studied in this work corresponds to a ferrimagnetic

<b>3 × 3</b>	<b>6 × 6</b>
$J_{2c-2c}$	$(\alpha_1 + \beta_1) \cdot 2$
$J_{3g-3g}$	$(\alpha_2 + 2\beta_2) \cdot 3$
$J_{\text{Gd-Gd}}$	$\alpha_3$
$J_{2c-3g}$	$6\gamma$
$J_{\text{Gd-2c}}$	$2\epsilon_1$
$J_{\text{Gd-3g}}$	$3\epsilon_2$

Table I. Relation between coefficients of matrices given in Eq. (15) and Eq. (16).

structure, i.e.,  $\mathbf{v}_{6 \times 6} = (m_{2c}, m_{2c}, m_{3g}, m_{3g}, m_{3g}, -m_{\text{Gd}})$ , where all the defined quantities are positive.  $J_{ss'}$  can be contracted to a  $3 \times 3$  matrix describing the same magnetic state,

$$J_{ss'}^{(3 \times 3)} = \begin{pmatrix} \frac{J_{2c-2c}}{2} & \frac{J_{2c-3g}}{2} & \frac{J_{\text{Gd-2c}}}{2} \\ \frac{J_{2c-3g}}{3} & \frac{J_{3g-3g}}{3} & \frac{J_{\text{Gd-3g}}}{3} \\ J_{\text{Gd-2c}} & J_{\text{Gd-3g}} & J_{\text{Gd-Gd}} \end{pmatrix}. \quad (15)$$

Note that we have used the same notation as introduced in reference [5]. Table I gives the relation of the coefficients in matrix  $J_{ss'}^{(3 \times 3)}$  with Eq. (14) such that the eigenvector of the former rightly is  $\mathbf{v}_{3 \times 3} = (m_{2c}, m_{3g}, -m_{\text{Gd}})$ . An additional contraction to a  $2 \times 2$  matrix can be done,

$$J_{ss'}^{(2 \times 2)} = \begin{pmatrix} J_{2c-2c} - \frac{1}{3}J_{3g-3g} + \frac{2}{3}J_{2c-3g} & J_{\text{Gd-3g}} - J_{\text{Gd-2c}} \\ 5(J_{\text{Gd-3g}} - J_{\text{Gd-2c}}) & J_{\text{Gd-Gd}} \end{pmatrix}, \quad (16)$$

with the eigenvector associated to the largest eigenvalue being  $\mathbf{v}_{2 \times 2} = (m_{\text{TM}}, -m_{\text{Gd}})$ . Eq. (16) is, however, an approximation for  $m_{\text{TM}} = m_{2c} \approx m_{3g}$ . We can now compare Eq. (10) and Eq. (16) with  $N_{\text{TM}} = 5$ . From  $-T(\partial S_i / \partial \mathbf{m}_i) = \mathbf{h}_i$  and

$$\begin{pmatrix} h_{\text{TM}} \\ h_{\text{Gd}} \end{pmatrix} = J_{ss'}^{(2 \times 2)} \cdot \begin{pmatrix} m_{\text{TM}} \\ m_{\text{Gd}} \end{pmatrix}, \quad (17)$$

it directly follows that

$$\begin{aligned} \gamma_{aa} &= \gamma_{\text{TM-TM}} \approx \frac{J_{2c-2c} - \frac{1}{3}J_{3g-3g} + \frac{2}{3}J_{2c-3g}}{2} \\ \gamma_{bb} &= \gamma_{\text{Gd-Gd}} \approx \frac{J_{\text{Gd-Gd}}}{2} \\ \gamma_{ab} &= \gamma_{\text{TM-Gd}} \approx J_{\text{Gd-3g}} - J_{\text{Gd-2c}}. \end{aligned} \quad (18)$$

See references [5, 50] for further detail.

### Condition for the critical point

Using Eq. (18), Eq. (16) can be rewritten in terms of the Gibbs free energy coefficients as

$$J_{ss'}^{(2 \times 2)} = \begin{pmatrix} 2\gamma_{\text{TM-TM}} & N_{\text{Gd}}\gamma_{\text{TM-Gd}} \\ N_{\text{TM}}\gamma_{\text{TM-Gd}} & 2\gamma_{\text{Gd-Gd}} \end{pmatrix}, \quad (19)$$

where we have reinstated  $N_{\text{TM}}$  and  $N_{\text{Gd}}$  for generality. At the critical point, the total net magnetization vanishes at all temperatures. At 0 K this condition requires  $N_{\text{TM}}\mu_{\text{TM}} = N_{\text{Gd}}\mu_{\text{Gd}}$ , whereas in the paramagnetic limit ( $T \rightarrow T_{\text{tr}}$ ) it imposes  $N_{\text{TM}}\mu_{\text{TM}}m_{\text{TM}} + N_{\text{Gd}}\mu_{\text{Gd}}m_{\text{Gd}} = 0$ . Combining these two relations with the fact that  $(m_{\text{TM}}, m_{\text{Gd}})$  is the eigenvector of Eq. (19), we obtain  $m_{\text{TM}} = -m_{\text{Gd}}$  and the condition for the critical point

$$\frac{2(\gamma_{\text{TM-TM}} - \gamma_{\text{Gd-Gd}})}{-\gamma_{\text{TM-Gd}}} = N_{\text{TM}} - N_{\text{Gd}}. \quad (20)$$

## DENSITY FUNCTIONAL THEORY CALCULATIONS

### *Ab initio* Magnetic interactions for GdCo<sub>5</sub>-type ferrimagnets

We calculate the isotropic pairwise interactions  $\{J_{ij}\}$  using the DFT-based Liechtenstein method [55], as implemented in the AkaiKKR package [66, 67], which employs the Korringa–Kohn–Rostoker (KKR) electronic structure method [68, 69]. The atomic sphere approximation (ASA) with values of the maximum angular momenta of  $l_{max} = 3$  and  $l_{max} = 2$  for the single-site scattering problem have been used for the Gd and TM sites, respectively. Our interest are the isotropic pairwise interactions so we stick to scalar relativistic calculations. We use the local density approximation as implemented by Moruzzi, Janak, and Williams [70] in combination with the "open core" scheme, in which the electronic structure is constrained to half-filled 4f-shell to fulfill Hund's rules.

In addition to the pristine material GdCo<sub>5</sub>, alloys of GdCo<sub>5-x</sub>TM<sub>x</sub> with TM: Ni, Cu, and Fe, as well as quaternary GdCo<sub>5-x</sub>(Fe<sub>0.5x</sub>Ni<sub>0.5x</sub>), have been studied by means of the coherent potential approximation (CPA) [58] assuming a homogenous distribution of the substituents on 2c and 3g crystallographic sites. Previous calculations have shown that the magnetic moment magnitudes are only weakly dependent on the location of TM dopants in the case of Ni, while their influence on the exchange constants may be more substantial [16], an effect that we leave for future investigations. The experimental lattice parameters of GdCo<sub>5</sub> from literature [47, 71] have been used for all material compositions.

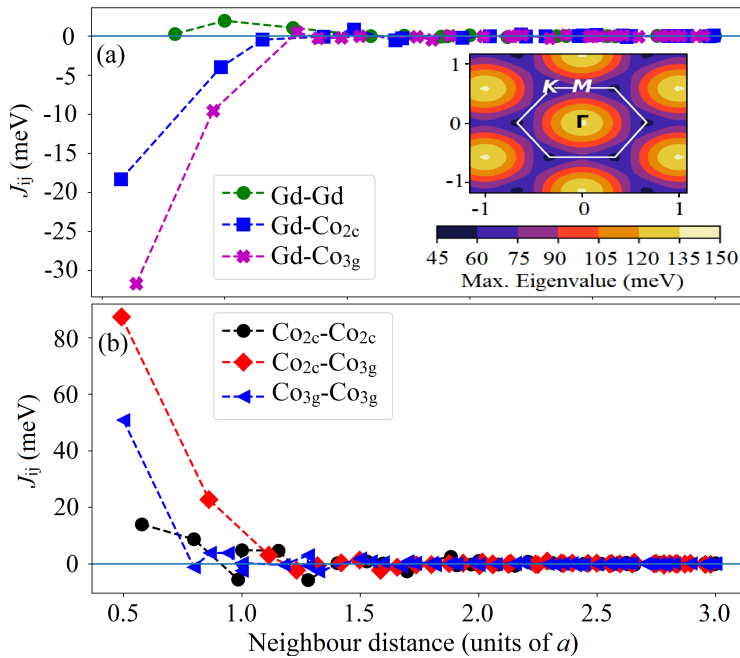


Figure 6. (a,b) Magnetic interactions  $J_{ij}^{\alpha\alpha'}$  computed for GdCo<sub>5</sub> as functions of the distance between the two atoms (in units of lattice constant  $a$ ). The Gd-Gd and Gd-Co interactions are shown in panel (a), while the Co-Co interactions are shown in panel (b). The inset shows the largest eigenvalue of the Fourier transform of the interaction matrix,  $J_{ss'}^{\alpha\alpha'}(\mathbf{q})$ , against the wave vector, see Eq. (5). Characteristic reciprocal lattice points of the Brillouin zone of a hexagonal close packed structure are shown (K, M, and  $\Gamma$ ).

Because the isotropic real-space parameters depend on the atomic species occupying the TM sites, they carry an additional index  $\alpha$  ( $\alpha'$ ) that specifies the substitutional element at site  $i$  ( $j$ ). Thus, the exchange interactions are written as  $J_{ij}^{\alpha\alpha'}(x)$ , where, for example,  $\alpha = \text{Co, Ni, Cu, or Fe}$  at the 2c and 3g sites. The distance dependency of the interactions are exemplified for GdCo<sub>5</sub> in Fig. 6. Importantly, these decay fast with the distance, being negligible up to the chosen cutoff of three lattice constants. The ferromagnetic Co-Co are the dominant interactions,  $\gamma_{\text{Gd-Gd}}$  therefore being much smaller than  $\gamma_{\text{TM-TM}}$  and  $\gamma_{\text{Gd-TM}}$  in Eq. (10) [see Eq. (18)].

The Fourier transform  $J_{ss'}^{\alpha\alpha'}(\mathbf{q})$ , see Eq. (5), allows to analyze the spectrum of favorable magnetic states. The inset of Fig. 6 shows the largest eigenvalue of  $J_{ss'}^{\alpha\alpha'}(\mathbf{q})$ , which gives the dominant instability of the paramagnetic state [50, 72]. This value peaks at  $\mathbf{q} = \mathbf{0}$  with eigenvector components describing antiparallel alignment between Gd and TM atoms

and confirms the stability of the assumed ferrimagnetic state.

### Electronic band structure and Fermi surface

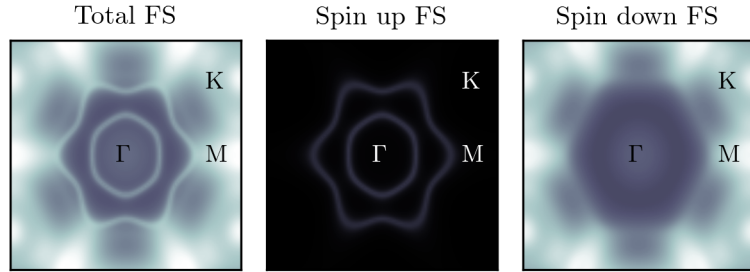


Figure 7. Total FS plot and its spin up and down components cut at  $k_z = 0$ . Characteristic reciprocal lattice points of the Brillouin zone of a hexagonal close packed structure are shown (K, M, and  $\Gamma$ ).

The electronic band-structure calculations presented in Fig. 4 of the main text were performed using the multiple-scattering Korringa–Kohn–Rostoker (KKR) method [73], as implemented in the Hutsepot code [74]. For completeness, Fig. 7 displays the corresponding Fermi surface of a representative GdCo<sub>5</sub>-type compound, providing a complementary view of the electronic structure.

### MONTE CARLO SIMULATIONS

Monte Carlo simulations for the Heisenberg Hamiltonian described in Eq. (3) containing the DFT-based  $\{J_{ij}^{\alpha\alpha'}\}$  are performed to validate our mean-field predictions. We employ the Mote Carlo code developed by Mavropoulos and coworkers [75, 76], designed to account for the effect of chemical disorder at each lattice site in alignment with the CPA. Anisotropy effects are not included within these Monte Carlo simulations. We construct  $12 \times 12 \times 12$  supercells, i.e. 19384 atoms. For each temperature we first equilibrate the system during 1000 Monte Carlo steps and then sample the thermodynamic properties for 5000 steps taking every 25 step into account. The phase transition temperature is determined by monitoring the peak of the heat capacity  $C_V^{\text{mag}} = \frac{1}{k_B T^2} (\langle E^2 \rangle - \langle E \rangle^2)$ , where  $E$  is the internal magnetic energy and  $\langle \dots \rangle$  denotes the average over Monte Carlo simulations.

Results are presented in Fig. 8. Pristine GdCo<sub>5</sub> lies close to the boundary separating the N-type and P-type phases, as indicated by its nearly compensated total magnetization  $M_{\text{tot}} \approx 0$  at  $T = 0$  K [see the light-colored curve in panel (a)]. Substitution in Gd(Co<sub>5-x</sub>TM<sub>x</sub>), with TM = Ni or Cu, initially leads to an increase in the compensation temperature  $T_{\text{comp}}$ , accompanied by a reduction in the maximum of  $M_{\text{tot}}(T)$  in the range  $T_{\text{comp}} < T < T_{\text{tr}}$ . At higher substitution levels, this trend culminates in an N-to-Q transition, where the compensation point disappears at  $T_{\text{tr}}$ , in agreement with previous experimental and theoretical studies [16].

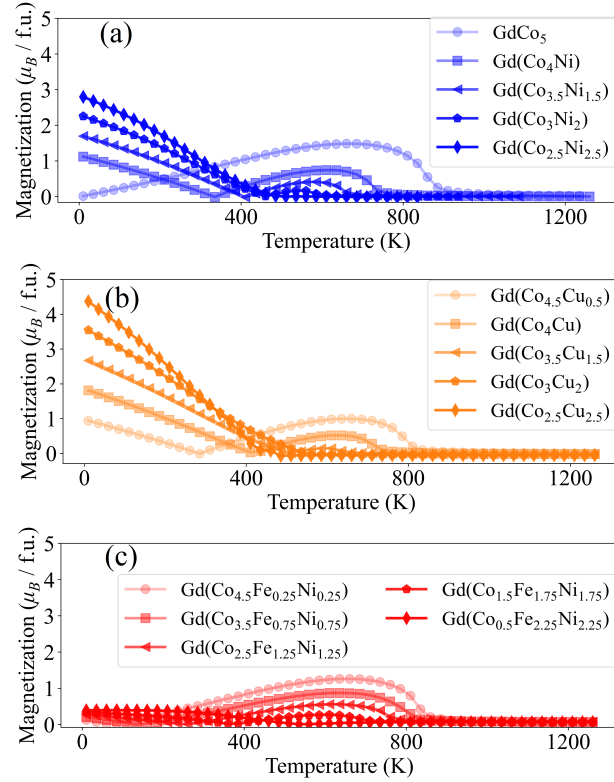


Figure 8. Temperature dependence of total magnetization of (a)  $\text{Gd}(\text{Co}_{5-x}\text{Ni}_x)$ , (b)  $\text{Gd}(\text{Co}_{5-x}\text{Cu}_x)$ , and (c)  $\text{Gd}(\text{Co}_{5-x}\text{Ni}_{0.5x}\text{Fe}_{0.5x})$  for increasing values of  $x$  from Monte Carlo simulations.

---

[1] Néel, M. Louis, “Propriétés magnétiques des ferrites ; ferrimagnétisme et antiferromagnétisme,” *Ann. Phys.* **12**, 137–198 (1948).

[2] J. Samuel Smart, “The Néel Theory of Ferrimagnetism,” *American Journal of Physics* **23**, 356–370 (1955).

[3] N. A. Spaldin, *Magnetic Materials: Fundamentals and Applications*, 2nd ed. (Cambridge University Press, 2010).

[4] Louis Néel, “Magnetism and Local Molecular Field,” *Science* **174**, 985–992 (1971).

[5] C. E. Patrick, S. Kumar, G. Balakrishnan, R. S. Edwards, M. R. Lees, E. Mendive-Tapia, L. Petit, and J. B. Staunton, “Rare-earth/transition-metal magnetic interactions in pristine and (Ni,Fe)-doped  $\text{YCo}_5$  and  $\text{GdCo}_5$ ,” *Phys. Rev. Materials* **1**, 024411 (2017).

[6] G. Sala and P. Gambardella, “Ferrimagnetic dynamics induced by spin-orbit torques,” *Advanced Materials Interfaces* **9**, 2201622 (2022).

[7] Li Liu, Yuzhou He, Yifei Ma, Peixin Qin, Hongyu Chen, Xiaoning Wang, Xiaorong Zhou, Ziang Meng, Guojian Zhao, Zhiyuan Duan, Dazhuang Kang, Yu Liu, Shuai Ning, Zhaochu Luo, Qinghua Zhang, and Zhiqi Liu, “Largely tunable compensation temperature in a rare-earth ferrimagnetic metal and deterministic spin-orbit torque switching for artificial neural network application,” *Journal of Materials Science & Technology* **234**, 15–23 (2025).

[8] Yue Zhang, Xueqiang Feng, Zhenyi Zheng, Zhizhong Zhang, Kelian Lin, Xiaohan Sun, Guanda Wang, Jinkai Wang, Jiaqi Wei, Pierre Vallobra, Yu He, Zixi Wang, Lei Chen, Kun Zhang, Yong Xu, and Weisheng Zhao, “Ferrimagnets for spintronic devices: From materials to applications,” *Applied Physics Reviews* **10**, 011301 (2023).

[9] M H Kryder, “Magneto-optical storage materials,” *Annual Review of Materials Research* **23**, 411–436 (1993).

[10] C. D. Stanciu, F. Hansteen, A. V. Kimel, A. Kirilyuk, A. Tsukamoto, A. Itoh, and Th. Rasing, “All-optical magnetic recording with circularly polarized light,” *Phys. Rev. Lett.* **99**, 047601 (2007).

[11] R. M. Grechishkin, M. S. Kustov, O. Cugat, J. Delamare, G. Poulin, D. Mavrudieva, and N. M. Dempsey, “Thermoreversible permanent magnets in the quasibinary  $\text{GdCo}_{5-x}\text{Cu}_x$  system,” *Applied Physics Letters* **89**, 122505 (2006).

[12] Changsoo Kim, Soogil Lee, Hyun-Gyu Kim, Ji-Ho Park, Kyung-Woong Moon, Jae Yeol Park, Jong Min Yuk, Kyung-Jin Lee, Byong-Guk Park, Se Kwon Kim, Kab-Jin Kim, and Chanyong Hwang, “Distinct handedness of spin wave across the compensation temperatures of ferrimagnets,” *Nature Materials* **19**, 980–985 (2020).

[13] C. E. Patrick and J. B. Staunton, “Rare-earth/transition-metal magnets at finite temperature: Self-interaction-corrected relativistic density functional theory in the disordered local moment picture,” *Phys. Rev. B* **97**, 224415 (2018).

[14] Roberto Moreno, Paula G. Bercoff, Unai Atxitia, Richard F. L. Evans, and Oksana Chubykalo-Fesenko, “Temperature dependence of exchange stiffness and energy barrier in compensated ferrimagnets,” *Phys. Rev. B* **111**, 184416 (2025).

[15] C. D. Stanciu, A. V. Kimel, F. Hansteen, A. Tsukamoto, A. Itoh, A. Kirilyuk, and Th. Rasing, “Ultrafast spin dynamics across compensation points in ferrimagnetic  $\text{GdFeCo}$ : The role of angular momentum compensation,” *Phys. Rev. B* **73**, 220402 (2006).

[16] A. L. Tedstone, C. E. Patrick, S. Kumar, R. S. Edwards, M. R. Lees, G. Balakrishnan, and J. B. Staunton, “Structural and magnetic properties of  $\text{GdCo}_{5-x}\text{Ni}_x$ ,” *Phys. Rev. Materials* **3**, 034409 (2019).

[17] Thomas A. Ostler, Richard F. L. Evans, Roy W. Chantrell, Unai Atxitia, Oksana Chubykalo-Fesenko, Ilie Radu, Radu Abrudan, Florin Radu, Arata Tsukamoto, A. Itoh, Andrei Kirilyuk, Theo Rasing, and Alexey Kimel, “Crystallographically amorphous ferrimagnetic alloys: Comparing a localized atomistic spin model with experiments,” *Phys. Rev. B* **84**, 024407 (2011).

[18] Igor I. Mazin and Klaus Koepernik and Michelle D. Johannes and Rafael González-Hernández and Libor Šmejkal, “Prediction of unconventional magnetism in doped  $\text{FeSb}_2$ ,” *Proceedings of the National Academy of Sciences* **118**, e2108924118 (2021).

[19] Libor Šmejkal, Jairo Sinova, and Tomas Jungwirth, “Emerging Research Landscape of Altermagnetism,” *Phys. Rev. X* **12**, 040501 (2022).

[20] Igor Mazin (The PRX Editors), “Editorial: Altermagnetism—A New Punch Line of Fundamental Magnetism,” *Phys. Rev. X* **12**, 040002 (2022).

[21] Libor Šmejkal, Jairo Sinova, and Tomas Jungwirth, “Beyond Conventional Ferromagnetism and Antiferromagnetism: A Phase with Nonrelativistic Spin and Crystal Rotation Symmetry,” *Phys. Rev. X* **12**, 031042 (2022).

[22] Ling Bai, Wanxiang Feng, Siyuan Liu, Libor Šmejkal, Yuriy Mokrousov, and Yugui Yao, “Altermagnetism: Exploring New Frontiers in Magnetism and Spintronics,” *Advanced Functional Materials* **34**, 2409327 (2024).

[23] Sang-Wook Cheong and Fei-Ting Huang, “Altermagnetism classification,” *npj Quantum Materials* **10**, 38 (2025).

[24] Rafael González-Hernández, Libor Šmejkal, Karel Výborný, Yuta Yahagi, Jairo Sinova, Tomáš Jungwirth, and Jakub Železný, “Efficient Electrical Spin Splitter Based on Nonrelativistic Collinear Antiferromagnetism,” *Phys. Rev. Lett.* **126**, 127701 (2021).

[25] Ching-Te Liao, Yu-Chun Wang, Yu-Cheng Tien, Ssu-Yen Huang, and Danru Qu, “Separation of Inverse Altermagnetic Spin-Splitting Effect from Inverse Spin Hall Effect in  $\text{RuO}_2$ ,” *Phys. Rev. Lett.* **133**, 056701 (2024).

[26] Lin-Ding Yuan, Zhi Wang, Jun-Wei Luo, Emmanuel I. Rashba, and Alex Zunger, “Giant momentum-dependent spin splitting in centrosymmetric low- $Z$  antiferromagnets,” *Phys. Rev. B* **102**, 014422 (2020).

[27] Satoru Hayami, Yuki Yanagi, and Hiroaki Kusunose, “Bottom-up design of spin-split and reshaped electronic band structures in antiferromagnets without spin-orbit coupling: Procedure on the basis of augmented multipoles,” *Phys. Rev. B* **102**, 144441 (2020).

[28] Makoto Naka, Yukitoshi Motome, and Hitoshi Seo, “Perovskite as a spin current generator,” *Phys. Rev. B* **103**, 125114

(2021).

[29] H. Bai, L. Han, X. Y. Feng, Y. J. Zhou, R. X. Su, Q. Wang, L. Y. Liao, W. X. Zhu, X. Z. Chen, F. Pan, X. L. Fan, and C. Song, “Observation of Spin Splitting Torque in a Collinear Antiferromagnet RuO<sub>2</sub>,” *Phys. Rev. Lett.* **128**, 197202 (2022).

[30] Shutaro Karube, Takahiro Tanaka, Daichi Sugawara, Naohiro Kadoguchi, Makoto Kohda, and Junsaku Nitta, “Observation of Spin-Splitter Torque in Collinear Antiferromagnetic RuO<sub>2</sub>,” *Phys. Rev. Lett.* **129**, 137201 (2022).

[31] Hamed Vakili, Edward Schwartz, and Alexey A. Kovalev, “Spin-Transfer Torque in Altermagnets with Magnetic Textures,” *Phys. Rev. Lett.* **134**, 176401 (2025).

[32] Yichi Zhang, Hua Bai, Jiankun Dai, Lei Han, Chong Chen, Shixuan Liang, Yanzhang Cao, Yingying Zhang, Qian Wang, Wenxuan Zhu, Feng Pan, and Cheng Song, “Electrical manipulation of spin splitting torque in altermagnetic RuO<sub>2</sub>,” *Nature Communications* **16**, 5646 (2025).

[33] Libor Šmejkal, Allan H. MacDonald, Jairo Sinova, Satoru Nakatsuji, and Tomas Jungwirth, “Anomalous Hall antiferromagnets,” *Nature Reviews Materials* **7**, 482–496 (2022).

[34] Gonzalez Betancourt, R. D. and Zubáč, J. and Gonzalez-Hernandez, R. and Geishendorf, K. and Šobáň, Z. and Springholz, G. and Olejník, K. and Šmejkal, L. and Sinova, J. and Jungwirth, T. and Goennenwein, S. T. B. and Thomas, A. and Reichlová, H. and Železný, J. and Kriegner, D., “Spontaneous Anomalous Hall Effect Arising from an Unconventional Compensated Magnetic Phase in a Semiconductor,” *Phys. Rev. Lett.* **130**, 036702 (2023).

[35] Helena Reichlova, Rafael Lopes Seeger, Rafael González-Hernández, Ismaila Kounta, Richard Schlitz, Dominik Kriegner, Philipp Ritzinger, Michaela Lammel, Miina Leiviskä, Anna Birk Hellenes, Kamil Olejník, Vaclav Petříček, Petr Doležal, Lukas Horak, Eva Schmoranzerova, Antonín Badura, Sylvain Bertaina, Andy Thomas, Vincent Baltz, Lise Michez, Jairo Sinova, Sebastian T. B. Goennenwein, Tomáš Jungwirth, and Libor Šmejkal, “Observation of a spontaneous anomalous Hall response in the Mn<sub>5</sub>Si<sub>3</sub> d-wave altermagnet candidate,” *Nature Communications* **15**, 4961 (2024).

[36] Libor Šmejkal, Anna Birk Hellenes, Rafael González-Hernández, Jairo Sinova, and Tomas Jungwirth, “Giant and Tunneling Magnetoresistance in Unconventional Collinear Antiferromagnets with Nonrelativistic Spin-Momentum Coupling,” *Phys. Rev. X* **12**, 011028 (2022).

[37] Guowei Yang, Zhanghuan Li, Sai Yang, Jiyuan Li, Hao Zheng, Weifan Zhu, Ze Pan, Yifu Xu, Saizheng Cao, Wenxuan Zhao, Anupam Jana, Jiawen Zhang, Mao Ye, Yu Song, Lun-Hui Hu, Lexian Yang, Jun Fujii, Ivana Vobornik, Ming Shi, Huiqiu Yuan, Yongjun Zhang, Yuanfeng Xu, and Yang Liu, “Three-dimensional mapping of the altermagnetic spin splitting in CrSb,” *Nature Communications* **16**, 1442 (2025).

[38] Sonka Reimers, Lukas Odenbreit, Libor Šmejkal, Vladimir N. Strocov, Prokopios Constantinou, Anna B. Hellenes, Rodrigo Jaeschke Ubiergo, Warley H. Campos, Venkata K. Bharadwaj, Atasi Chakraborty, Thibaud Denneulin, Wen Shi, Rafal E. Dunin-Borkowski, Suvadip Das, Mathias Kläui, Jairo Sinova, and Martin Jourdan, “Direct observation of altermagnetic band splitting in CrSb thin films,” *Nature Communications* **15**, 2116 (2024).

[39] Jianyang Ding, Zhicheng Jiang, Xiuhua Chen, Zicheng Tao, Zhengtai Liu, Tongrui Li, Jishan Liu, Jianping Sun, Jinguang Cheng, Jiayu Liu, Yichen Yang, Runfeng Zhang, Liwei Deng, Wenchuan Jing, Yu Huang, Yuming Shi, Mao Ye, Shan Qiao, Yilin Wang, Yanfeng Guo, Donglai Feng, and Dawei Shen, “Large Band Splitting in g-Wave Altermagnet CrSb,” *Phys. Rev. Lett.* **133**, 206401 (2024).

[40] Cong Li, Mengli Hu, Zhilin Li, Yang Wang, Wanyu Chen, Balasubramanian Thiagarajan, Mats Leandersson, Craig Polley, Timur Kim, Hui Liu, Cosma Fulga, Maia G. Vergniory, Oleg Janson, Oscar Tjernberg, and Jeroen van den Brink, “Topological Weyl altermagnetism in CrSb,” *Communications Physics* **8**, 311 (2025).

[41] Banik Rai, Krishnendu Patra, Satyabrata Bera, Sk Kalimuddin, Kakan Deb, Mintu Mondal, Priya Mahadevan, and Nitesh Kumar, “Direction-Dependent Conduction Polarity in Altermagnetic CrSb,” *Advanced Science* **12**, 2502226 (2025).

[42] Zheyuan Liu, Makoto Ozeki, Shinichiro Asai, Shinichi Itoh, and Takatsugu Masuda, “Chiral Split Magnon in Altermagnetic MnTe,” *Phys. Rev. Lett.* **133**, 156702 (2024).

[43] O. J. Amin, A. Dal Din, E. Golias, Y. Niu, A. Zakharov, S. C. Fromage, C. J. B. Fields, S. L. Heywood, R. B. Cousins, F. Maccherozzi, J. Krempaský, J. H. Dil, D. Kriegner, B. Kiraly, R. P. Campion, A. W. Rushforth, K. W. Edmonds, S. S. Dhesi, L. Šmejkal, T. Jungwirth, and P. Wadley, “Nanoscale imaging and control of altermagnetism in MnTe,” *Nature* **636**, 348–353 (2024).

[44] Libor Šmejkal, Rafael González-Hernández, T. Jungwirth, and J. Sinova, “Crystal time-reversal symmetry breaking and spontaneous Hall effect in collinear antiferromagnets,” *Science Advances* **6**, eaaz8809 (2020).

[45] Yichen Liu, San-Dong Guo, Yongpan Li, and Cheng-Cheng Liu, “Two-Dimensional Fully Compensated Ferrimagnetism,” *Phys. Rev. Lett.* **134**, 116703 (2025).

[46] Peng-Jie Guo, Huan-Cheng Yang, Xiao-Yao Hou, Ze-Feng Gao, Wei Ji, and Zhong-Yi Lu, “Luttinger-compensated bipolarized magnetic semiconductor,” *Phys. Rev. B* **112**, L180405 (2025).

[47] Y.C. Chuang, C.H. Wu, T.C. Li, S.C. Chang, and M.S. Wang, “Structure and magnetic properties of Gd(Co<sub>1-x</sub>Ni<sub>x</sub>)<sub>5</sub> compounds,” *Journal of the Less Common Metals* **78**, 219 (1981).

[48] R.J. Radwański, “Anisotropic ferrimagnets in high magnetic fields,” *Physica B+C* **142**, 57–64 (1986).

[49] Rolf Stinshoff, Ajaya K. Nayak, Gerhard H. Fecher, Benjamin Balke, Siham Ouardi, Yurii Skourski, Tetsuya Nakamura, and Claudia Felser, “Completely compensated ferrimagnetism and sublattice spin crossing in the half-metallic Heusler compound Mn<sub>1.5</sub>FeV<sub>0.5</sub>Al,” *Phys. Rev. B* **95**, 060410 (2017).

[50] E. Mendive-Tapia and J. B. Staunton, “Ab initio theory of the Gibbs free energy and a hierarchy of local moment correlation functions in itinerant electron systems: The magnetism of the Mn<sub>3</sub>A materials class,” *Phys. Rev. B* **99**, 144424 (2019).

[51] J. B. Staunton, R. Banerjee, M. dos Santos Dias, A. Deak, and L. Szunyogh, “Fluctuating local moments, itinerant electrons, and the magnetocaloric effect: Compositional hypersensitivity of FeRh,” *Phys. Rev. B* **89**, 054427 (2014).

[52] Eduardo Mendive-Tapia, Jörg Neugebauer, and Tilmann Hickel, “Ab initio calculation of the magnetic gibbs free energy of materials using magnetically constrained supercells,” *Phys. Rev. B* **105**, 064425 (2022).

[53] Eduardo Mendive-Tapia and Julie B. Staunton, “Theory of magnetic ordering in the heavy rare earths: Ab initio electronic origin of pair- and four-spin interactions,” *Phys. Rev. Lett.* **118**, 197202 (2017).

[54] See Supplemental Material for further details on the modelling framework underlying the Gibbs free energy, computational details about the DFT calculations and Monte Carlo simulations, and the relation between the Gibbs free energy parameters and the isotropic pairwise interactions.

[55] A. I. Liechtenstein, M. I. Katsnelson, V. P. Antropov, and V. A. Gubanov, “Local spin density functional approach to the theory of exchange interactions in ferromagnetic metals and alloys,” *Journal of Magnetism and Magnetic Materials* **67**, 65 – 74 (1987).

[56] R.J. Radwański, J.J.M. Franse, P.H. Quang, and F.E. Kayzel, “The Gd anisotropy in GdCo<sub>5</sub>,” *Journal of Magnetism and Magnetic Materials* **104-107**, 1321–1322 (1992), proceedings of the International Conference on Magnetism, Part II.

[57] R.J. Radwański, “Anisotropic ferrimagnets in high magnetic fields,” *Physica B+C* **142**, 57–64 (1986).

[58] P. Soven, “Coherent-Potential Model of Substitutional Disordered Alloys,” *Phys. Rev.* **156**, 809–813 (1967).

[59] K. H. J. Buschow and M. Brouha, “Narrow Bloch walls in the RCo<sub>5</sub>-type rare-earth–cobalt compounds,” *Journal of Applied Physics* **47**, 1653–1656 (1976).

[60] L.A.S. de Oliveira, J.P. Sinnecker, R. Grössinger, A. Pentón-Madrigal, and E. Estévez-Rams, “Cu induced coercivity enhancement in the low viscosity GdCo<sub>5-x</sub>Cu<sub>x</sub> system,” *Journal of Magnetism and Magnetic Materials* **323**, 1890–1894 (2011).

[61] Rui Zhang, Yangkun He, Daniel Fruchart, J.M.D. Coey, and Zsolt Gercsi, “Rare-earth-free noncollinear metallic ferrimagnets Mn<sub>4-x</sub>Z<sub>x</sub>N with compensation at room temperature,” *Acta Materialia* **234**, 118021 (2022).

[62] L Prendeville, P Jiménez-Cavero, A Naden, Yangkun He, K Rode, Z Gercsi, and J M D Coey, “Magnetic compensation in sputtered ferrimagnetic Mn<sub>4-x</sub>Ga<sub>x</sub>N thin films,” *Journal of Physics D: Applied Physics* **57**, 355005 (2024).

[63] B L Gyorffy, A J Pindor, J Staunton, G M Stocks, and H Winter, “A first-principles theory of ferromagnetic phase transitions in metals,” *Journal of Physics F: Metal Physics* **15**, 1337–1386 (1985).

[64] R. P. Feynman, “Slow Electrons in a Polar Crystal,” *Phys. Rev.* **97**, 660–665 (1955).

[65] Minoru Takahashi, “Generalization of mean-field approximations by the feynman inequality and application to long-range ising chain,” *Journal of the Physical Society of Japan* **50**, 1854–1860 (1981).

[66] H. Akai, “Electronic Structure Ni–Pd Alloys Calculated by the Self-Consistent KKR-CPA Method,” *Journal of the Physical Society of Japan* **51**, 468–474 (1982), <http://kkr.issp.u-tokyo.ac.jp>.

[67] H. Akai, “Fast Korringa-Kohn-Rostoker coherent potential approximation and its application to FCC Ni-Fe systems,” *Journal of Physics: Condensed Matter* **1**, 8045–8064 (1989).

[68] J. Korringa, “On the calculation of the energy of a Bloch wave in a metal,” *Physica* **13**, 392–400 (1947).

[69] W. Kohn and N. Rostoker, “Solution of the Schrödinger Equation in Periodic Lattices with an Application to Metallic Lithium,” *Phys. Rev.* **94**, 1111–1120 (1954).

[70] V.L. Moruzzi, J.F. Janak, and A.R. Williams, “II - CALCULATIONS,” in *Calculated Electronic Properties of Metals*, edited by V.L. Moruzzi, J.F. Janak, and A.R. Williams (Pergamon, 1978) pp. 11 – 22.

[71] A.V. Andreev and S.M. Zadvorkin, “Thermal expansion and spontaneous magnetostriction of RCo<sub>5</sub> intermetallic compounds,” *Physica B: Condensed Matter* **172**, 517 – 525 (1991).

[72] Eduardo Mendive-Tapia, Manuel dos Santos Dias, Sergii Grytsiuk, Julie B. Staunton, Stefan Blügel, and Samir Lounis, “Short period magnetization texture of B20-MnGe explained by thermally fluctuating local moments,” *Phys. Rev. B* **103**, 024410 (2021).

[73] H Ebert, D Ködderitzsch, and J Minár, “Calculating condensed matter properties using the KKR-Green’s function method—recent developments and applications,” *Reports on Progress in Physics* **74**, 096501 (2011).

[74] M Däne, M Lüders, A Ernst, D Ködderitzsch, W M Temmerman, Z Szotek, and W Hergert, “Self-interaction correction in multiple scattering theory: application to transition metal oxides,” *21*, 045604 (2009).

[75] M. Matsumoto and T. Nishimura, “Mersenne Twister: A 623-Dimensionally Equidistributed Uniform Pseudo-Random Number Generator,” *ACM Trans. Model. Comput. Simul.* **8**, 3–30 (1998).

[76] M. Ležaić, P. Mavropoulos, G. Bihlmayer, and S. Blügel, “Exchange interactions and local-moment fluctuation corrections in ferromagnets at finite temperatures based on noncollinear density-functional calculations,” *Phys. Rev. B* **88**, 134403 (2013).